ACS APPLIED MATERIALS & INTERFACES

www.acsami.org Research Article

Role of Oxygen Source on Buried Interfaces in Atomic-Layer-Deposited Ferroelectric Hafnia–Zirconia Thin Films

Hanan Alexandra Hsain,* Younghwan Lee, Suzanne Lancaster, Monica Materano, Ruben Alcala, Bohan Xu, Thomas Mikolajick, Uwe Schroeder, Gregory N. Parsons, and Jacob L. Jones*

Cite This: *ACS Appl. Mater. Interfaces* 2022, 14, 42232−42244 Read Online

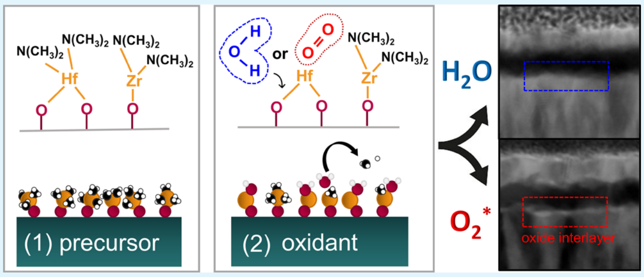

ABSTRACT: Hafnia−zirconia (HfO_2−ZrO_2) solid solution thin films have emerged as viable candidates for electronic applications due to their compatibility with Si technology and demonstrated ferroelectricity at the nanoscale. The oxygen source in atomic layer deposition (ALD) plays a crucial role in determining the impurity concentration and phase composition of HfO_2−ZrO_2 within metal−ferroelectric−metal devices, notably at the $Hf_{0.5}Zr_{0.5}O_2$ /TiN interface. The interface characteristics of HZO/TiN are fabricated via sequential no-atmosphere processing (SNAP) with either H_2O or O_2-plasma to study the influence of oxygen source on buried interfaces. Time-of-flight secondary ion mass spectrometry reveals that HZO films grown via O_2-plasma promote the development of an interfacial TiO_x layer at the bottom HZO/TiN interface. The presence of the TiO_x layer leads to the development of 111-fiber texture in HZO as confirmed by two-dimensional X-ray diffraction (2D-XRD). Structural and chemical differences between HZO films grown via H_2O or O_2-plasma were found to strongly affect electrical characteristics such as permittivity, leakage current density, endurance, and switching kinetics. While HZO films grown via H_2O yielded a higher remanent polarization value of 25 $\mu C/cm^2$, HZO films grown via O_2-plasma exhibited a comparable P_r of 21 $\mu C/cm^2$ polarization and enhanced field cycling endurance limit by almost 2 orders of magnitude. Our study illustrates how oxygen sources (O_2-plasma or H_2O) in ALD can be a viable way to engineer the interface and properties in HZO thin films.

KEYWORDS: *$Hf_{0.5}Zr_{0.5}O_2$, hafnia, zirconia, ferroelectric, orthorhombic, oxygen, texture*

I. INTRODUCTION

Although the 100th anniversary of the discovery of ferroelectricity was recently celebrated,[1] ferroelectricity in HfO_2 has been intensively studied only for the last 10 years. In that time, ferroelectricity has been achieved in HfO_2 using numerous deposition techniques[2] and incorporated into applications such as ferroelectric nonvolatile memories,[3] ferroelectric tunnel junctions,[4] supercapacitors and pyroelectric energy harvesters,[5,6] and brain-inspired neuromorphic computing.[7] The reason for such a breadth of applications for HfO_2 thin films lies in certain material properties, e.g., high bandgap energy (>5 eV), complementary metal-oxide-semiconductor (CMOS) compatibility, and most recently, its ability to demonstrate ferroelectricity at the nanoscale.[8] The polymorphs of HfO_2 (and isostructural ZrO_2) include monoclinic ($P2_1/c$), tetragonal ($P42/nmc$), cubic ($Fm\bar{3}m$), and orthorhombic ($Pca2_1$) where polymorphs can be described by a distorted parent pseudo-cubic reference frame. The origin of ferroelectricity in HfO_2 has been ascribed to the polar orthorhombic phase (s.g. $Pca2_1$).[9] While not predicted to be stable at room temperature in the classical HfO_2 temperature−pressure phase diagram,[2,10] the polar orthorhombic phase can be stabilized by surface energy effects at low film thicknesses (<30 nm)[11] but also in bulk material (5 mm).[12] In addition, the solid solution of HfO_2−ZrO_2 can give rise to dielectric, ferroelectric, and antiferroelectric properties by simply altering the Hf/Zr ratio.[3,13] Alloying HfO_2 films with ZrO_2 has the additional advantage of lowering the crystallization temperature to 370 °C for 30 nm films, which can help to mitigate the appearance of the deleterious nonferroelectric phase (e.g., monoclinic), which often forms at higher temperatures.[14] Here, we focus our attention on the 1:1 Hf/Zr HZO composition, which is reported to have the highest ferroelectric response.[15,16]

Ferroelectric HZO thin films are often fabricated via atomic layer deposition (ALD) where an appropriate combination of metalorganic precursor and oxygen source is required to deposit high-quality inorganic films. Several studies have highlighted the effect of different oxygen sources such as O_2-plasma, H_2O, and O_3 on electrical properties[17−21] but few have

Received: June 21, 2022
Accepted: August 29, 2022
Published: September 7, 2022

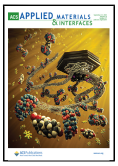

https://doi.org/10.1021/acsami.2c11073

Table 1. Tabulated Properties of HZO and HfO_2-Based Capacitors via ALD with Different Oxygen Sources Reported in the Literature

material	thickness [nm]	precursor	dep T [°C]	oxygen source	GPC (nm/cycle)	anneal [°C]	P_r [$\mu C/cm^2$]	leakage current density [A/cm^2] at 2V	relative permittivity	fatigue limit	ref
HZO (50:50)	10	Cp-Hf[$N(CH_3)_2]_3$ and Cp-Zr[$N(CH_3)_2]_3$	300	O_2*	0.92	450 for 20 s	22.5	N/A	26	10^5 at 4 MV/cm	20
HZO (50:50)	10	Cp-Hf[$N(CH_3)_2]_3$ and Cp-Zr[$N(CH_3)_2]_3$	300	O_3	0.82	450 for 20 s	21.0	N/A	24	10^6 at 4 MV/cm	20
HfO_2	11	TEMA-Hf	300	H_2O	0.75	650 for 20 s	N/A	1×10^{-9}	22	N/A	17
HfO_2	20	TEMA-Hf	300	O_2*	1.5	650 for 20 s	N/A	2×10^{-8}	21.5	N/A	17
HfO_2	N/A	TEMA-Hf	300	O_3	0.95	650 for 20 s	N/A	3×10^{-8}	22	N/A	17
HfO_2	N/A	$HfCl_4$	300	H_2O	1.05	850	N/A	N/A	N/A	N/A	18
HfO_2	N/A	$HfCl_4$	300	O_2*	1.10	850	N/A	N/A	N/A	N/A	18
HZO (50:50)	10	TDMA-Hf TDMA-Zr	250	H_2O	N/A	400 for 60 s N_2	19	10^{-2}	N/A	10^7 at 2 MV/cm	21
HZO (50:50)	10	TDMA-Hf TDMA-Zr	250	O_3	N/A	400 for 60 s N_2	23	10^{-4}	N/A	10^7 at 2 MV/cm	21
HZO (50:50)	10	TDMA-Hf TDMA-Zr	270	H_2O	0.95	800 for 30 s N_2	25	10^{-4}	N/A	2×10^4 at 3 MV/cm	this work
HZO (50:50)	10	TDMA-Hf TDMA-Zr	270	O_2*	0.95	800 for 30 s N_2	21	5×10^{-5}	N/A	10^7 at 3 MV/cm	this work

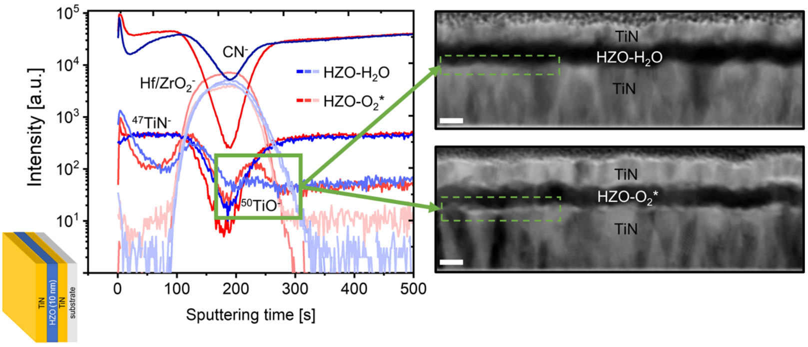

Figure 1. Chemical characterization of TiN/HZO/TiN MFM capacitors. (a) ToF-SIMS depth profile of HZO-H_2O and HZO-O_2* films showing chemical species HfO_2^-, ZrO_2^-, $^{47}TiN^-$, CN^-, and $^{50}TiO^-$. High-angle annular bright-field (HAABF) images of (b) HZO-H_2O and (c) HZO-O_2* films annealed at 800 °C for 30 s. The white scale bar is equivalent to 10 nm.

considered the effects of ALD oxygen source on ferroelectric properties and interface within the metal−ferroelectric−metal (MFM) stack. The few representative studies investigating the effect of different oxygen sources on the electrical and ferroelectric properties of HZO are listed in Table 1. For example, Alcala et al. studied the effects of using either O_2-plasma (designated herein as O_2*) or ozone (O_3) as an oxidant source on 10 nm HZO films, both of which demonstrated comparable remanent polarization values near 21 $\mu C/cm^2$.[20] While O_3 and O_2* are viable reactants for producing HfO_2 with ALD, highly reactive oxygen sources or plasmas may be less favorable, for example, due to potential damage during deposition on organic substrates, or due to difficulty achieving ideal uniformity on high-aspect-ratio, three-dimensional structures. Therefore, the development of robust ALD processes using different oxygen sources must be considered for different applications. Kim et al. grew 10 nm HZO films via thermal ALD with H_2O, which resulted in devices with a $P_r \sim 19\ \mu C/cm^2$ comparable to films processed with O_3, which generated a $P_r \sim 24\ \mu C/cm^2$. Kim et al. posited that hydrogen incorporation and additional carbon contamination using H_2O led to more degradation of ferroelectric properties compared to films processed with O_3.[21] Though both the works of Alcala et al. and Kim et al. shed light on the influence of oxygen source on the ferroelectric properties of HZO, the reports do not uncover the role of the oxygen source in interfacial properties, specifically the preferred orientation of HZO when in contact with its electrode. Recent transmission electron microscopy (TEM) studies have revealed that a strong orientational alignment is present between HfO_2-based films with underlying TiN electrodes,[22] while other studies have highlighted that differences in interfacial oxidation in differently processed samples could affect the alignment and accordingly change the phase formation in the ferroelectric layer.[23,24] X-ray photoelectron spectroscopy (XPS) studies by Hamouda et al. and Baumgarten et al. revealed the importance of processing conditions such as annealing temperature and deposition method on the physical chemistry and oxygen vacancy concentration at the TiN/HZO interface.[25,26] It follows that the choice of oxygen source used in ALD could be an important processing factor in engineering the structure−property relationships in HZO/TiN devices.

Here, we elucidate the influence of using either O_2* or H_2O as the oxygen source during ALD on the interface characteristics of the TiN/HZO/TiN capacitor. We perform detailed structural (e.g., crystallographic texture, onset crystallization temperature, chemical quality within HZO and at the interface of HZO/TiN) and electrical (permittivity, leakage current, endurance, switching kinetics) measurements to assess the merits of using either O_2* or H_2O during ALD. Unique to our study, we grow capacitors via sequential, no-atmosphere processing (SNAP), where exposure to the ambient air is minimized by maintaining vacuum during every layer deposition, which has been found to reduce spontaneous oxidation and carbon contamination. We find that ALD growth via O_2* results in HZO films with less carbon impurities and a more pronounced TiO_x interfacial layer, which affects the development of 111-fiber texture in HZO. The presence of an additional TiO_x layer in O_2*-processed HZO is found to strongly influence electrical behaviors such as remanent polarization, leakage, permittivity, endurance, and switching kinetics. Overall, the results here demonstrate that altering the ALD oxygen source can impact the interfacial formation and the selection of oxygen source can be leveraged in the design of future ferroelectric HZO thin-film devices.

II. METHODS

MFM stacks consisting of TiN/HZO/TiN were deposited onto SiO_2/Si substrates (VA semiconductors) after the substrates were rinsed using isopropanol and acetone. The MFM stack was composed from bottom to top: Si wafer/30 nm TiN/10 nm HZO/10 nm TiN and was deposited sequentially without breaking vacuum during ALD (Ultratech/Cambridge Fiji G2) using the sequential, no-atmosphere processing (SNAP)[16] procedure. The precursors used for this process were tetrakis(dimethylamido)-hafnium(IV) (TDMAH), tetrakis-(dimethylamido)-zirconium(IV) (TDMAZ), and tetrakis-(dimethylamido)-titanium(IV) (TDMAT), and either water (H_2O) or oxygen plasma (O_2*) as the oxygen source. These multilayer capacitors are referred to here as HZO-H_2O and HZO-O_2*, referencing the use of either H_2O or O_2-plasma as the oxygen source, respectively. For TiN deposition, a gas flow of 110 sccm argon was used to deliver the precursors and oxygen source into the ALD chamber and Ar:N_2 of 10:20 sccm was used to generate plasma for TiN deposition. The temperatures for all precursors, delivery line, and chamber were maintained at 75°, 150°, and 270 °C, respectively. TiN deposition was accomplished via plasma-enhanced ALD using 250 W plasma power for a period of 20 s, where 430 cycles were pulsed at a growth rate of ~0.6 Å/cycle. For ALD of HZO, the N_2 purge pressure was maintained at 10 mTorr and precursor, and oxygen reactant half-cycles were pulsed at a pressure of 150−130 mTorr. For thermal ALD of H_2O-based HZO, Hf/Zr precursors were pulsed for 0.25 s followed by a 5 s purge time, and then 0.1 s H_2O was pulsed followed by a 5 s purge time. For PE-ALD of HZO-O_2*, Hf and Zr precursors were pulsed for 0.25 s followed by 20 sccm of O_2-plasma at 300 W for 6 s. Alternating cycles of Hf and Zr precursors were pulsed for 100 cycles with an approximate growth rate of 1.0 Å/cycle to obtain a 1:1

Table 2. XPS Elemental Quantification of the Surface of 10 nm HZO-H_2O and HZO-O_2* Films on Si Annealed at 800 °C

	oxygen (O 1s) [atom %]	carbon (C 1s) [atom %]	zirconium (Zr 3d) [atom %]	hafnium (Hf 4f) [atom %]	(Hf 4f + Zr 3d)/O 1s
HZO-H_2O	51.2 ± 0.8	19.8 ± 0.5	15.9 ± 0.1	13.2 ± 0.1	0.56
HZO-O_2*	54.4 ± 0.9	14.4 ± 0.4	16.5 ± 0.1	14.7 ± 0.1	0.57

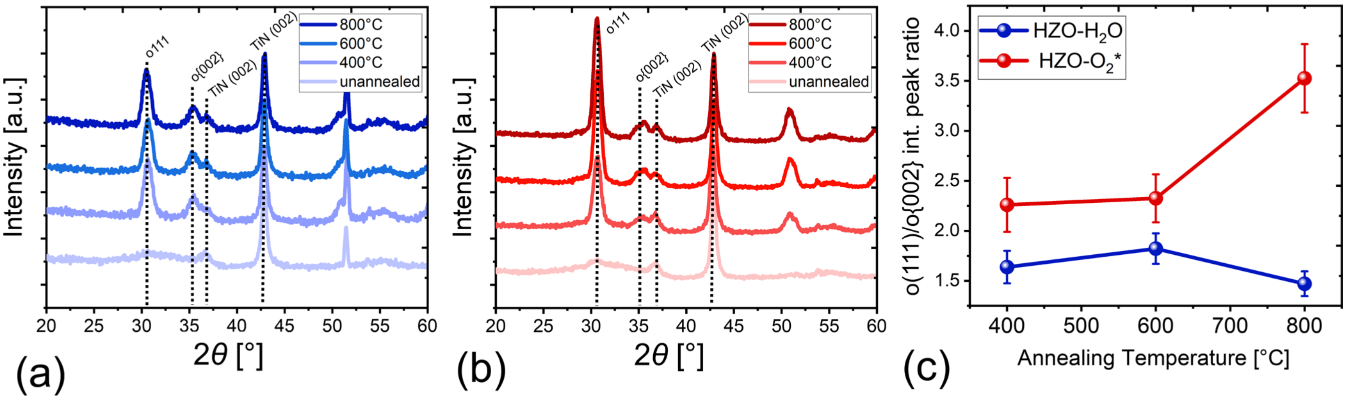

Figure 2. GIXRD patterns for films annealed at 400, 600, or 800 °C processed with (a) H_2O or (b) O_2*. Intensities are normalized to the 002 reflection of TiN; (c) ratio of integrated peak areas of o(111)/o{002} reflection of polar orthorhombic HZO ($Pca2_1$) as a function of annealing temperature for films processed with H_2O (blue) or O_2* (red). Reference orthorhombic HZO from PDF #: 04-005-5597.

composition of an approximately ~10 nm HZO thin film. The thickness was confirmed via ellipsometry with a standard model for HZO and TiN. MFM structures were then annealed via rapid thermal annealing (AnnealSys AS-One) with a ramp rate of 10 °C/s to 400, 600, and 800 °C with a hold time of 30 s.

For electrical characterization, circular contact pads of 200 μm diameter with 10 nm Ti/30 nm Pt were deposited via e-beam evaporation through a shadow mask. MFM samples were subsequently etched using a modified Standard Cleaning 1 (SC1) etch H_2O:30% H_2O_2:30% NH_4OH 50:2:1 at 50 °C for 5 min. Ferroelectric characterization was conducted using an aixACCT System TF Analyzer 3000, where each measurement was conducted on a pristine contact with no previous electrical history. For polarization−electric field (P−E) loops, hysteresis measurements were taken using a bipolar triangular waveform at 1 kHz and an electrical field of 1−4 MV/cm. The endurance measurement was conducted using a periodic square waveform with 100 kHz and an electric field of 3 and 3.5 MV/cm, while five P−E measurements were captured per decade on a log scale. Capacitance versus voltage measurements were also measured on the aixACCT using a bipolar small-signal capacitance−voltage measurement with a voltage sweep up to 3 V with a 50 mV small-signal amplitude at 10 kHz.

Experimental details for analytical characterization including grazing incidence X-ray diffraction (GIXRD), X-ray photoelectron spectroscopy (XPS), time-of-flight secondary ion mass spectrometry (ToF-SIMS), transmission electron microscopy (TEM), and scanning electron microscopy (SEM) are included in the Supporting Information.

III. RESULTS AND DISCUSSION

To investigate the chemical nature of TiN/HZO/TiN MFM stacks as a function of layer depth, ToF-SIMS depth profiles were acquired for films grown with either H_2O or O_2*. The spectra for both films are overlaid in Figure 1a with blue and red lines corresponding to HZO-H_2O and HZO-O_2*, respectively. In both spectra, HfO_2^- and ZrO_2^- species were evenly distributed in the middle layer and $^{47}TiN^-$ species were sandwiched on either side of the HZO layer. There are several notable differences between the ToF-SIMS spectra of HZO-O_2* and HZO-H_2O. First, the intensity of the CN^- signal within the HZO layer is more than 10 times larger in HZO-H_2O films compared to HZO-O_2* films. Higher carbon concentration was expected for films processed with H_2O due to the lower oxidizing power of water over O_2-plasma.[27] Though ToF-SIMS allows for the relative comparison of chemical species, given the probabilistic nature of the ion yield, this analytical method does not provide exact atomic concentration of various chemical species. XPS was employed to determine the atomic concentration of Hf, Zr, O, N, Ti, and C of a 10 nm HZO film processed with either H_2O or O_2-plasma and annealed at 800 °C for 30 s. Fitting the survey spectra generated the elemental quantification shown in Table 2, which confirmed the higher atomic percentage of carbon species in HZO-H_2O (19.8 atom %) compared to HZO-O_2* (14.4 atom %), as well as a slightly lower hafnium concentration of 13.2 atom % versus 14.7 atom %, respectively, which implies that O_2-plasma produces a more complete ALD reaction and allows for a higher removal of organic ligands during the purge cycle. High-resolution spectra for Hf 4f, Zr 3d, O 1s, and C 1s are shown in Figure S1 and confirm the trends noted from the survey scans. Note that the high carbon concentration found by XPS is not only due to the presence of unreacted ligands from ALD metalorganic precursors, but also accounts for adsorbed hydrocarbons from exposure to the atmosphere. The XPS quantification is consistent with our previous depth profiling XPS work, which suggested ~20 atom % C on the surface of the film, which decreases to <5 atom % when measured via depth profiling XPS within the MFM stack.[16]

Finally, ToF-SIMS reveals that HZO-O_2* films have a higher $^{50}TiO^-$ intensity at both oxide-electrode interfaces compared to HZO-H_2O films. Given that the bottom electrode is more susceptible to oxidation during the ALD growth of the overlaying oxide, the higher intensity of the $^{50}TiO^-$ species, especially at the bottom TiN/HZO interface in HZO-O_2*, suggests that using O_2-plasma at our specific ALD growth conditions generates a more pronounced interfacial titanium oxide.

The presence of an interfacial TiO_x layer in HZO-O_2* was also confirmed via TEM (Talos F200X G2). Figure 1b,c shows high-angle annular bright-field (HAABF) images for HZO-

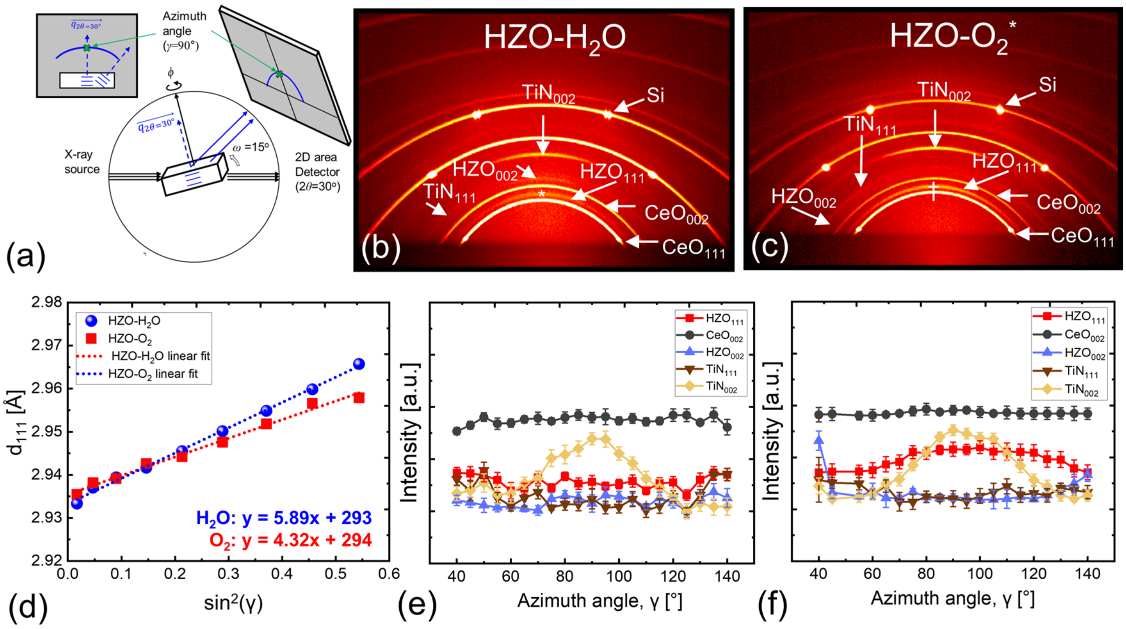

Figure 3. Two-dimensional X-ray diffraction (2D-XRD) characterization for texture analysis of HZO-H_2O and HZO-O_2* annealed at 800 °C for 30 s. (a) Schematic of X-ray geometry where scattering vector q is perpendicular to sample surface at $2\theta = 30°$, $\gamma = 90°$, $\Omega = 15°$ at a distance of 50 mm and 120 s exposure time. (b, c) 2D-XRD image of HZO-H_2O and HZO-O_2*, where star and cross symbol represent $\gamma = 90°$. (d) Residual stress analysis using a modified $\sin^2(\psi)$ approach plotted with lattice constant for the orthorhombic (111) plane (d_{111}) for HZO-H_2O (blue circles) and HZO-O_2 (red squares). (e, f) Integrated area of selected peaks as a function of azimuth angle for HZO-H_2O and HZO-O_2, respectively.

H_2O and HZO-O_2*, respectively. The thickness of the top TiN, HZO, and bottom TiN layers for both films was found to be approximately 10, 10, and 30 nm, respectively, consistent with ellipsometry measurements. Higher scattering is expected from materials composed of heavier elements, whereas materials with lighter atomic mass allow for incident electrons to penetrate more easily; thus, we expect to see high scattering from the higher atomic mass and crystalline HZO layer compared to the lighter TiO_x. Figure 1b shows an interface in HZO-H_2O with very minimal oxidation. On the other hand, Figure 1c shows a more pronounced and concentrated light layer at the bottom HZO/TiN interface which is consistent with the presence of a sub-1-nm-thick TiO_x layer in HZO-O_2*. Taken together, ToF-SIMS, XPS, and TEM results indicate that growing HZO films via PE-ALD using O_2-plasma promotes the preferential growth of a thicker interfacial TiO_x layer on the bottom TiN electrode and minimizes carbon contamination within the HZO layer relative to thermal ALD using H_2O.

Given the differing HZO/TiN bottom electrode interfaces present in the HZO-H_2O and HZO-O_2* film stacks, it was hypothesized that the oxygen source used during ALD may impact the microstructure of the films. GIXRD patterns for HZO-H_2O and HZO-O_2* HZO capacitors annealed at 400, 600, or 800 °C are shown in Figure 2a,b, respectively. Intensities are normalized to the integrated area of 002 TiN to better perceive the intensity differences among films while the diffraction geometry was kept constant across all measurements. All films crystallized at temperatures as low as 400 °C based on the appearance of several diffraction peaks. The peak at $2\theta \sim 30.3°$ is ascribed to the orthorhombic 111 (herein referred to as o111) and the peak at $2\theta \sim 35.6°$ corresponds to a combination of the orthorhombic 200, 020, and 002 reflections (collectively referred to as o{200}). It should be noted that the literature typically reports the peaks at $2\theta \sim$ 30.3 and 35.6° as, respectively, a combination of the overlapping orthorhombic (PDF #: 04-005-5597) and tetragonal (PDF #: 04-011-8820) phases; however, no evidence for antiferroelectric behavior typically attributed to the presence of the tetragonal phase was found in the present study and so only the orthorhombic phase is considered. In both HZO-O_2* and HZO-H_2O, no monoclinic phase was observed even after higher annealing temperatures of 800 °C. A sharp peak near 52° observed in HZO-H_2O can be ascribed to the 311 reflection from the Si wafer.

It is interesting to note the higher relative intensity of the o111 peak in HZO-O_2* compared to that of HZO-H_2O after all annealing temperatures. In particular, the integrated peak area of o111 for the HZO-O_2* is over 2 times larger than the integrated peak area of o111 for the HZO-H_2O at 800 °C; meanwhile, the o{002} peak for HZO-H_2O has approximately the same integrated area and intensity as the o{002} peak in HZO-O_2*. The differences in the relative peak areas between HZO-H_2O and HZO-O_2* may be interpreted as either: (1) a difference in overall orthorhombic phase fraction; or (2) differences in preferred crystallographic orientation, i.e., texture. In our case, we ascribe the peak area differences between HZO-H_2O and HZO-O_2* to differences in texture, explained as follows. From the reference XRD pattern, each of relative intensities of the orthorhombic 200, 002, and 020 reflections are reported as 12−14% compared to the maximum intensity of the orthorhombic 111 reflection. According to the reference XRD pattern of orthorhombic HZO, if the film had a smaller overall orthorhombic phase fraction, then one would expect to see a concurrent decrease in the intensity of the o111 along with the o{002} peak. However, this is not the case; instead, the integrated area corresponding to the o{002} peak in HZO-H_2O is comparable to the integrated area corresponding to the o{002} peak in HZO-O_2*. Meanwhile, the o111 peak is smaller in HZO-H_2O compared to HZO-O_2*. Thus,

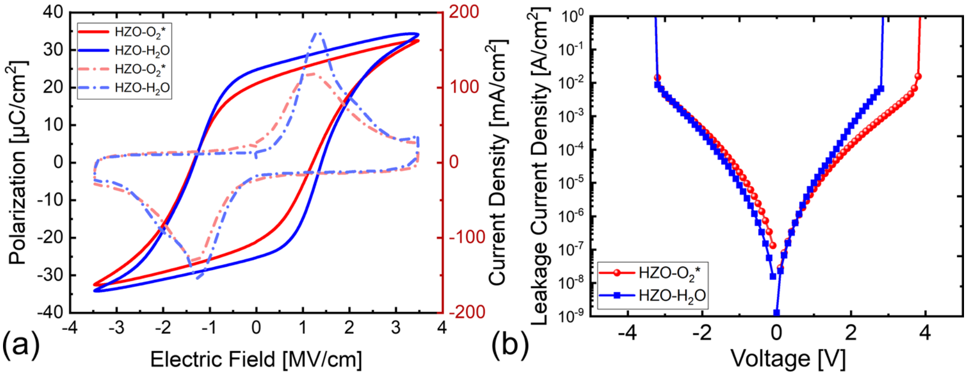

Figure 4. Electrical characterization of HZO fabricated with H_2O (blue) and O_2-plasma (red). (a) Polarization versus electric field, (b) leakage current density versus voltage ($I-V$).

the observed differences in o111 integrated area are likely due to differences in texture present in HZO-H_2O and HZO-O_2* films.

To better assess possible differences in texture in the two films and their structural evolution with temperature, a semiquantitative texture analysis was performed on HZO-H_2O and HZO-O_2* films in which the ratios of the integrated peak areas for o111 versus o{002} were compared. Figure 2c shows the calculated ratio as a function of annealing temperature. Each peak was fit to a Pearson-VII model profile shape function using LIPRAS software (not shown).[28] The o111/o{002} ratio increases as a function of annealing temperature for HZO-O_2* while the ratio stays fairly constant for HZO-H_2O. At any given annealing temperature, the o111/o{002} ratio is lower for HZO-H_2O than for HZO-O_2*. The increase of o111/o{002} ratio in HZO-O_2* indicates increased diffraction from planes contributing to o111 rather than o{002}. Given that the thickness of both films is nearly the same, the increased diffraction intensity is attributed to an increased fraction of preferentially oriented diffracting planes. In other words, there are specific planes most aligned perpendicular to the scattering vector (e.g., (111) of orthorhombic and not the o{002} planes) for HZO-O_2* annealed at 800 °C. GIXRD analysis suggests that processing films with different oxygen sources result in differences in preferred orientation between HZO-H_2O and HZO-O_2* films. Given the evidence for texture differences between HZO-H_2O and HZO-O_2*, 2D-XRD measurements are conducted to further characterize the degree of preferred orientation in films annealed at 800 °C.

HZO-H_2O and HZO-O_2* films are investigated via 2D-XRD using an area detector (D8 Venture) for texture characterization. The goniometer geometry is illustrated in Figure 3a and the Debye−Scherrer rings collected from HZO-H_2O and HZO-O_2* are shown in Figure 3b,c, respectively. The 2D-XRD image was segmented in the azimuth direction to reduce 2D data into one-dimensional (1D) line patterns for subsequent analysis. Selected peaks of HZO, TiN, and CeO_2 were integrated over 2θ using LIPRAS and then plotted as a function of azimuth angle (γ) from 40 to 140°. Further details concerning texture analysis including calibration with CeO_2 is included in the Supporting Information. In polycrystalline films that are randomly oriented, minimal change in intensity should be observed as a function of azimuth angle, γ. Thus, given the strong intensity variation of the TiN 002 peak as a function of γ with a maximum at $\gamma = 90°$ the TiN electrode is 001-textured in both HZO-H_2O and HZO-O_2*. Meanwhile, we notice that all other peak intensities in HZO-H_2O are relatively constant with γ except for the o{002} peak which shows a small increase near γ = 70−110° which is consistent with weak 001-fiber texture. The low peak intensity can be explained by considering the structure factor of orthorhombic HZO where the relative intensities of the orthorhombic 200, 002, and 020 reflections are individually only ∼12−14% of the maximum intensity of the orthorhombic 111 reflection. In HZO-O_2*, the o111 peak shows a relatively strong intensity variation as a function of γ consistent with 111-fiber texture. 2D-XRD analysis is therefore consistent with the interpretation that the development of a thicker interfacial TiO_x layer in HZO-O_2* breaks the texture transference from 001-textured TiN and instead leads to the development of 111-textured HZO.

TEM studies have shown a strong orientation alignment between underlying TiN and HZO suggesting that the role of HZO/TiN interface may affect the crystallographic orientation of overlaying HZO.[29] Specifically, the influence of oxygen source on preferred crystallographic orientation in HfO_2 thin films has also been previously reported in the literature. Aarik et al. observed differences in reflection intensities in HfO_2 films processed with $HfCl_4$ and either O_3 or H_2O where the latter oxygen source demonstrated preferred growth in the [001] direction.[18] Aarik et al. ascribed the preferred orientation in H_2O-processed films to originate from the selective formation of hydroxyl groups on certain crystallographic planes. In our study, one possibility for the differences in HZO texture found in HZO-H_2O and HZO-O_2* films may be due to the differences in the bottom HZO/TiN interface. As shown in Figure 1, HZO-O_2* possesses a more pronounced TiO_x layer than HZO-H_2O. Given that the bottom TiN used in our MFM capacitors is strongly 001-textured,[16] the inclusion of a TiO_x layer may render an "interface-breaking" effect, i.e., a disruption in how the underlying 001-textured TiN may influence the formation of the texture of HZO. The interface-breaking of TiN/HZO in HZO-O_2* could thus encourage the growth of more energetically favorable HZO {111} planes which have a lower surface energy compared to the {001} planes.[30] Due to the direct contact between the bottom TiN electrode and HZO-H_2O film, inheritance of an 001 texture from the TiN to the HZO layer may occur more readily which would result in higher o{002} intensities relative to o111 found in Figure 2a.

The biaxial stress state was assessed in both HZO films using a modified $\sin^2(\psi)$ approach,[31] where both films were assumed to exhibit isotropic elastic behavior. The observed changes in d-spacing were plotted as a function of $\sin^2(\psi)$ where γ was used as a near approximation to ψ for convenience. The d-spacing of CeO_2 was not found to vary as a function of γ, which confirms that the variation of d_{111} for HZO-H_2O and HZO-O_2* are not experimental artifacts. Additional details regarding the biaxial stress calculation can be found in the Supporting Information. Figure 3d shows lattice spacing plotted as a function of $\sin^2(\gamma)$. Using the slopes of the linear fit ($R^2 \sim 1$) the in-plane biaxial stress for HZO-H_2O and HZO-O_2 was calculated to be 4.2 ± 0.4 and 3.1 ± 0.3 GPa, respectively. The linearity of the fit agrees with a biaxial stress state that lacks shear components. The biaxial stress value matches well with Fields et al. who calculated the biaxial stress for a 20 nm film of $Hf_{0.54}Zr_{0.46}O_2$ to be 4.71 ± 0.4 GPa.[32] Such large in-plane tensile stresses in HZO are consistent with other reports which claim that the stresses are a combined result of processing steps and thermal expansion mismatch between the HZO film and the underlying substrate.[33,34] The higher biaxial stress experienced by HZO-H_2O may be explained by an interface characterized by more direct contact with TiN which has a larger thermal expansion coefficient ($\alpha = 10.27 \times 10^{-6}$ °C^{-1})[35] than TiO_2 ($\alpha = 8.42 \times 10^{-6}$ °C^{-1}).[36] The larger mismatch in thermal expansion coefficient with HZO and underlying TiN may have resulted in a larger in-plane biaxial stress state in HZO-H_2O. Previous studies have suggested that tensile strain imposed by the underlying substrate may distort the tetragonal cell and preferentially stabilize the orthorhombic phase in HZO;[24,37] thus, the ferroelectric properties are expected to be impacted by the difference in biaxial stress values found in HZO-H_2O and HZO-O_2.

Figure 4 shows the electrical characterization of HZO-H_2O and HZO-O_2* films after rapid thermal annealing at 800 °C for 30 s. Figure 4a displays the polarization versus electric-field (P−E) loop and current density versus electric-field (J−E) for HZO-H_2O (blue) and HZO-O_2* (red), which are used to extract the remanent polarization (P_r) value at 0 MV/cm. Note that several P−E loops were obtained for each capacitor and that Figure 4a illustrates a representative loop for each capacitor in its pristine state, i.e., no previous cycling. The extracted P_r values for HZO-H_2O and HZO-O_2* are 25 and 21 $\mu C/cm^2$, respectively. Thus, the use of O_2* during ALD growth of HZO films is found to slightly decrease the remanent polarization value relative to films grown using the H_2O source. The lower P_r observed in HZO-O_2* contrasts with several other studies that found HZO films produced with stronger oxidizers (either O_3 or O_2*) led to a higher remanent polarization value (see Table 1). The slightly lower P_r observed in HZO-O_2* is likely due to conditions related to the unique SNAP fabrication of the MFM structure. Unlike conventional fabrication where TiN and HZO layers are deposited in separate chambers which requires vacuum breaking steps, HZO-H_2O and HZO-O_2* capacitors are grown sequentially within the ALD reactor without breaking vacuum. Thus, the interface of HZO-H_2O is especially pristine, i.e., lower oxidation and contamination, because it has not been exposed to ambient air which has been shown to introduce adventitious carbon and oxidation and diminish the properties of the device. Therefore using a stronger oxidant during ALD lessens the effects of no-atmosphere deposition by generating an unintentional TiO_x layer. The slightly higher P_r observed in HZO-H_2O, on the other hand, may stem from a more pristine interface, or conversely, the lack of TiO_x growth.[38] The additional TiO_x could impact HZO-O_2* in several different ways such as (1) by causing a slight voltage drop across the interface film and reducing the field on the HZO layer when the same external voltage is used, (2) by altering the oxygen vacancy concentration leading to slightly different phase composition, and/or (3) by promoting the development of crystallographic texture which alters the film's out-of-plane polarization in response to an electric field applied perpendicular to the surface of the film. Oxygen vacancies are known to help stabilize the formation of the orthorhombic phase by reducing the free energy of formation, reducing the grain size, or providing additional nucleation sites in HZO thin films.[39,40] The observed higher P_r in HZO-H_2O compared to HZO-O_2 could be attributed to the difference in oxygen concentration where more oxygen vacancies may exist in HZO-H_2O due to the lower oxidizing power of H_2O compared to O_2-plasma. XPS analysis of the O 1s spectra confirms the lower oxygen content in HZO-H_2O, whereas ToF-SIMS indicated a higher concentration of the TiO_x oxide at the bottom interface of HZO-O_2*. Since oxygen vacancies are often generated when gettering TiN is in contact with HfO_2,[41] the additional TiO_x interfacial layer in HZO-O_2* allows Ti to react with excess oxygen from the interface and thus mitigates oxygen diffusion and vacancy formation in HZO. The presence of the TiO_x layer may also act as a physical barrier and inhibit the exchange of O and N between TiN/HZO, inhibiting N-doping and/or oxygen vacancy formation in HZO-O_2*.[42]

The third factor that may be responsible for the diminished P_r observed in HZO-O_2* is the 111-fiber textured HZO layer as was suggested by 2D-XRD analysis. It is understood that the spontaneous polarization vector (P_s) of orthorhombic HZO (s.g. $Pca2_1$) lies along the c-axis and is parallel to the [001] direction. Because P_s is not aligned parallel to the field direction in an ideally oriented crystallite with a <111> oriented normal to the film as found in HZO-O_2*, a higher field is theoretically required to switch the same number of domains in the HZO-O_2* sample compared to the more preferentially oriented HZO-H_2O. In summary, the slightly diminished P_r found in HZO-O_2* may be explained by several factors originating from the more pronounced TiO_x layer, which could alter the voltage drop across the capacitor, diminished oxygen vacancy concentration within the film, and/or promoted 111-texture in HZO, which is not optimally oriented in the direction of P_s, thus causing an observable reduction in P_r.

The coercive field is expected to be higher in HZO-O_2* due to the factors described above, i.e., voltage drop and less favorable texture for switching induced by the presence of TiO_x. However, Figure 4a shows that the $+|E_c|$ is measured to be 1.1 and 1.4 MV/cm for HZO-O_2* and HZO-H_2O, respectively. The slightly lower $+|E_c|$ in HZO-O_2* can be understood by considering the effect of a nonferroelectric on the E_c and tilt of the P−E loop.[38,43,44] Tagantsev et al. showed that the pinching and tilt of the hysteresis loop in bulk ceramics is an indicator of a passive layer residing between the ferroelectric layer and electrode, where the passive layer is related to the slope of the P−E loop via the following relationship

$$\frac{d}{L\varepsilon_d} \sim \frac{E_c\varepsilon_o}{P_r} \qquad (1)$$

where d is the thickness of the passive layer, L is the thickness of the ferroelectric layer, E_c is the coercive field, ε_d is the relative permittivity of the passive layer, and ε_0 is the vacuum

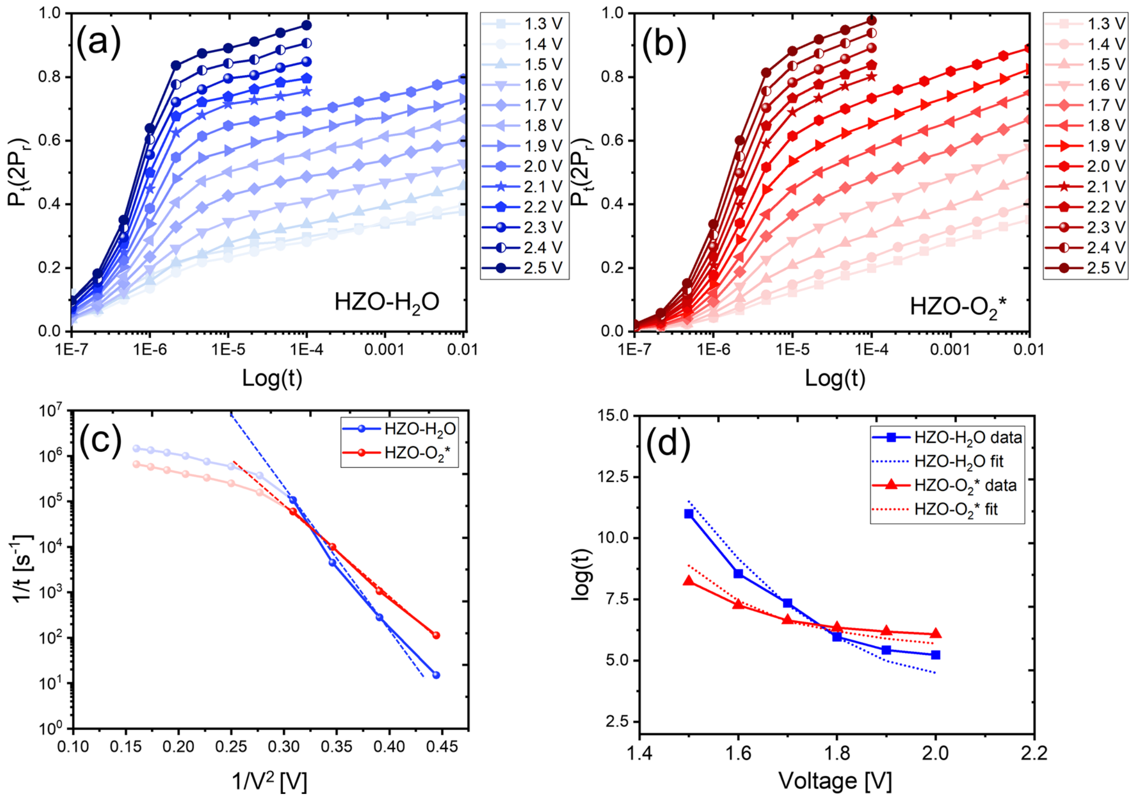

Figure 5. Switching kinetics measurements for (a) HZO-H_2O and (b) HZO-O_2*. (c) Data extracted from 50% total switched polarization and fitted to $1/t$ versus $1/V^2$ relationship, where t and V are the time and voltage necessary to switch 50% of the $P_{r,max}$ plotted for both films, respectively. (d) Log(t) versus V relationship used to extract the activation voltage V_o for both films.

permittivity. Therefore, according to the Tagantsev et al. model, the greater tilting of the P−E loop and lower E_c in the case of the HZO-O_2 originates from the depolarization field generated by the thicker passivating layer at the HZO/TiN interface in HZO-O_2*.

Figure 4b shows the leakage current density as a function of applied electric field (I−V) for HZO-H_2O and HZO-O_2* films taken in their pristine state, i.e., noncycled. Both films show a generally low leakage current density of 10^{-5} A/cm^2 near the coercive field of ∼1.0 MV/cm. We note, however, that HZO-O_2* shows an asymmetrical I−V curve, i.e., applying positive DC bias tends to yield a lower leakage current density and higher dielectric breakdown endurance compared to the negative DC bias region. The observed asymmetry in the I−V curve for HZO-O_2* provides further evidence of an asymmetrical interface where higher growth of TiO_x at the bottom HZO/TiN interface may have resulted in a preferential voltage drop across the bottom dielectric interface.[45] Such a voltage drop could lead to the observed lower leakage current density and increase the breakdown field limit (+2.7 versus +4.0 MV/cm for HZO-H_2O and HZO-O_2*, respectively).

To further elucidate the impact of ALD oxygen source on ferroelectric device properties, the kinetics of polarization reversal are investigated for HZO-H_2O and HZO-O_2*. Figure 5a,b displays the speed of switching as a function of pulse amplitude and width for HZO-H_2O and HZO-O_2*, respectively. Experimental methods follow closely with Materano et al.[46] and details concerning the pulse train can be found in the Supporting Information. In bulk or epitaxial ferroelectric materials, switching behavior follows the Kolmogorov−Avrami−Ishibashi (KAI) model, which describes the nucleation and propagation of reversed domains where the gate voltage follows a simple power law.[47] It has been shown that polycrystalline ferroelectrics deviate from the KAI model given their higher impurity concentration and interface-governed nucleation switching. In thin-film ferroelectric-metal capacitors, domain nucleation typically occurs at the interface and/or at one- or two-dimensional defects, which act as heterogeneous nucleation sites.[48] Domain nuclei may grow at these sites and propagation becomes energetically favorable once a critical nucleus size has been reached. Therefore, the nucleation event rather than domain propagation is the limiting factor for domain switching. In that case, the Du-Chen model, built upon the Nucleation Limited Switching (NLS) model, becomes suitable for describing frequency-dependent polarization switching.[49] Based on the Du-Chen free energy model and classical nucleation theory, Mulaosmanovic et al.[50] derived the following expression for the average nucleation waiting time

$$\tau = \tau_o \exp\left(\frac{\alpha}{k_B T} * \frac{1}{(V - V_o)^2}\right) \tag{2}$$

where τ_o and α are material-dependent constants that represent the shortest nucleation time and a thermodynamic contribution related to domain wall energy and switching portions in the film, respectively; k_B is the Boltzmann constant; T is the temperature; and V_o is the activation voltage. Equation 2 can be rewritten to show that a linear relationship between log(τ) and $1/V^2$ should exist and can allow for the material constants τ_o and α to be extracted from the intercept and slope, respectively. A strong linearity of $1/t$ versus $1/V^2$ in Figure 5c in the range of $0.32 < 1/V^2 < 0.45$ indicates that the

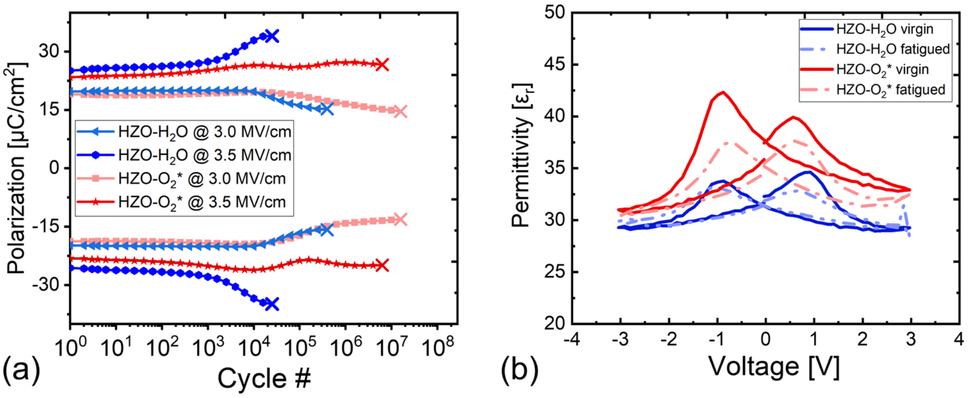

Figure 6. Endurance measurements for HZO-H_2O (blue) and HZO-O_2* (red). (a) Fatigue measurements at 3.0 and 3.5 MV/cm and (b) small-signal permittivity for pristine and fatigued capacitors cycled at 3.0 MV/cm for 10^6 and 10^4 cycles for HZO-H_2O and HZO-O_2* respectively.

data fit well to eq 2 for both HZO-H_2O and HZO-O_2*. Note that the nonlinearity found at values of $1/V^2 < 0.32$ (shaded region) corresponds to an RC delay at high voltages and short times.[46] Within the linear region, a lower slope is observed for HZO-O_2* relative to HZO-H_2O which indicates that the impact of the applied field on domain nucleation is smaller for HZO-O_2*, while the minimum switching time τ_o is lower for the HZO-H_2O film.

To extract the activation voltage V_o, the dependence between switching voltages is plotted against pulse time for 50% total realizable switched polarization in Figure 5d. Fitting the data to eq 2, the activation voltages V_o are calculated to be 1.0 ± 0.05 and 1.15 ± 0.07 V for HZO-H_2O and HZO-O_2*, respectively. These values are in good agreement with other reports which typically cite a V_o within the range of the coercive field of ∼ 1 MV/cm for 10 nm HfO_2 films.[46,51] It is interesting to note here that the E_c of HfO_2 films is unusually high, whereas in conventional ferroelectric materials, e.g., $PbTiO_3$, the E_c is typically one-tenth of the activation field (E_a ∼ V_o for 10 nm film).[52,53] Typically, polarization occurs via nucleation and propagation of reversed domains. Due to the collective behavior of domain switching, the E_c is generally reduced by a factor equivalent to the width of the domain wall.[54] In HfO_2 thin films, however, the domain walls are vanishingly thin and do not contribute to the reduction of the coercive field. Lee et al. showed that weakly interacting domain walls and zero group velocity of the polar modes in HfO_2 cause the domain walls to only propagate inefficiently by hopping over a large energy barrier. Thus, reversing the polarization of a single layer was found to be nearly energetically equivalent (per layer) to reversing the polarization of all layers giving rise to scale-free ferroelectricity in HfO_2.[53]

The lower activation energy for domain switching in HZO-H_2O is consistent with the observed faster τ in Figure 5 up to ∼ 5×10^{-4} s after which τ becomes faster for HZO-O_2*. The observed lower V_o in HZO-H_2O may be due to a higher defect concentration, i.e., carbon impurities, within HZO which provides more nucleation sites for switching events to occur according to the NLS model. To explain the larger activation barrier V_o and the higher voltage required to switch HZO-O_2* at short waiting times, we consider the interface of HZO/TiN. In HZO-O_2* an additional interfacial oxide is present which acts as an activation barrier for domain nucleation due to the voltage drop across the ferroelectric. While this effect is prominent for short waiting times, at a critical time ∼5×10^{-4} s, enough charge injection into the interfacial layer has occurred that the field becomes saturated; as a result, polarization switching becomes less dependent on applied field.[55,56] In addition, the TiO_x layer not only acts as a physical resistive element, reducing the voltage drop across the ferroelectric, but it also breaks the influence of the 001 texture in the underlying TiN on the HZO film texture. As was reported by Lee et al., the spontaneous polarization vector is tilted 55° away from normal in 111-textured domains in HZO films, whereas in 001-textured HZO films, the spontaneous polarization of domains is parallel to the normal direction.[57] This means that with a field amplitude applied parallel to the induced spontaneous polarization direction, the HZO-H_2O film with a higher fraction of 001-oriented poles is more favorably oriented in line with the polarization axis. Thus, domain switching is more energetically favorable in HZO-H_2O which explains the lower activation barrier for switching at shorter waiting times. Comparatively, HZO-O_2* only begins to experience faster switching at longer time scales where the switching probability becomes less voltage-dependent. To explain this, we consider that ferroelastic switching in 111-fiber textured films is less constrained by the substrate than in randomly oriented or 001-oriented films.[58,59] The theoretically lower in-plane clamping effect in HZO-O_2* is consistent with the lower in-plane biaxial stress, σ_{22}, determined via the modified $\sin^2(\psi)$ method. Thus, once a saturating field over the additional TiO_x has been achieved, the lowered mechanical constraint of 111-textured HZO-O_2* allows for faster switching.

The two effects of the TiO_x layer described here, i.e., acting as an additional interfacial resistive/capacitive element and promoting preferential 111-textured domains in HZO, both reduce the overall electric field contribution applied on switching domains within the HZO layer in HZO-O_2* and leads to the macroscopically observed higher activation barrier for switching. In the case of HZO-H_2O, switching is more energetically favorable, i.e., lower V_o, which may be due to its preferentially oriented domains for switching, or the presence of more defects as observed in ToF-SIMS and XPS. At longer waiting times, switching becomes faster in HZO-O_2* due to the saturated field across the TiO_x and the lower mechanical boundary constraints. In terms of applications, the oxygen source ought to be coupled strategically to the intended functionality. For ferroelectric random access memory (FE-RAM) applications, HZO-O_2* would be the more advantageous choice due to its higher switching speeds at operating voltages ∼2.5 V.[60,61] Therefore, the influence of oxygen source on switching kinetics should be carefully considered and selected depending on the desired end-use requirements.

Endurance characteristics, i.e., the remanent polarization as a function of cycle number for HZO-H_2O and HZO-O_2* taken at 3.0 and 3.5 MV/cm cycling fields, are displayed in Figure 6a. The magnitude of $\pm P_r$ is relatively stable for both HZO-H_2O and HZO-O_2* until 10^3 cycles, suggesting little to no wake-up effect. The endurance limit (number of cycles until breakdown) decreases for both HZO-H_2O and HZO-O_2* when subjected to a higher cycling field of 3.5 MV/cm. After 10^3 cycles at 3.5 MV/cm, the increase in polarization in HZO-H_2O is likely due to electrostatic charge injection for repetitive field cycling until dielectric breakdown.[62] HZO-O_2* at 3.0 and 3.5 MV/cm and HZO-H_2O at 3.5 MV/cm experience a diminishing of P_r after a certain number of cycles and the closure of the memory window (difference between positive and negative remanent polarization) which is a signature of fatigue onset. Several fatigue mechanisms plague the ferroelectric HfO_2 system including domain pinning,[62] seed inhibition,[63] and the formation of the passive dead layer.[38] Generally, it is believed that dielectric degradation in ferroelectric HZO occurs when electric field cycling leads to charge injection leading to an increase in defect generation where subsequent charge trapping causes the ferroelectric to experience a lower effective field. The lower electric field across the ferroelectric reduces the number of domains that are able to participate in switching and leads to the observed diminished P_r.[64]

Generally, the endurance limit of HZO-O_2* was found to be higher than HZO-H_2O for both cycling fields (~10^7 versus ~10^5 cycles, respectively). To explain the increased endurance limit in HZO-O_2* we consider the additional interfacial TiO_x layer and the higher oxygen concentration found in HZO-O_2*. Given that a common fatigue mechanism experienced in HZO involves the generation of defects (possibly oxygen vacancies), which modify the internal field and switching properties of the capacitor, an excess oxygen supply at the interface of HZO-O_2* may balance the oxygen vacancy generation during field cycling. Conversely, higher oxygen vacancy concentrations in HZO-H_2O could also lead to a more rapid accumulation of defects during cycling and lead to faster breakdown. An additional factor influencing the endurance may stem from the differences in carbon impurity concentration between HZO-H_2O and HZO-O_2* where a higher carbon concentration was found in HZO-H_2O due to unreacted metalorganic ligands from incomplete ALD reaction. It is well known that higher defect concentrations (and leakage current density) are correlated with poor endurance properties in HZO-based capacitors.[65,66] Thus if a slight decrease in remanent polarization may be tolerated, interface engineering via PE-ALD with O_2-plasma can be a viable route for increasing the endurance limit and decreasing the leakage current density in ferroelectric HZO films.

Figure 6b shows the dielectric permittivity-versus electric field (ε_r-E) for HZO-H_2O and HZO-O_2* in their virgin and cycled states. The permittivity at saturating DC field (~3 MV/cm) is $\varepsilon_r \sim 30$ for both films, which suggests a predominately orthorhombic phase as reported in the literature where the theoretical permittivity $\varepsilon_r \sim 30$ of orthorhombic HZO is closely isotropic.[67] The ε_r value extracted from the small-signal permittivity measurements at saturating fields agrees well with GIXRD data where a predominate composition of orthorhombic phase was observed for both films. At the extrinsic region near the coercive field ~1 MV/cm the maximum permittivity field is 37.5 and 47.5 for HZO-H_2O and HZO-O_2*, respectively. The higher permittivity observed in HZO-O_2* suggests enhanced domain wall mobility and/or a faster nucleation rate which would be consistent with observations from high field switching kinetics measurements. Heightened permittivity at the coercive field may be explained by the larger ferroelastic domain wall contribution in HZO-O_2* due to reduced mechanical clamping as a result of 111-textured HZO caused by the oxidized metal/oxide interface. Both HZO-H_2O and HZO-O_2* showed a relatively stable permittivity value at the maximum applied field but a decrease in permittivity at low fields after applied fatigue cycling at 3.0 MV/cm. The trend of consistent permittivity at saturating fields and lower permittivity at low fields suggests that field cycling impacts the extrinsic contributions (domain walls) and does not strongly impact intrinsic contributions (phase composition). In typical ferroelectric HZO films possessing some wake-up, domains initially locked in a preferential polarization state become de-pinned after electronic charges and related defects redistribute across the ferroelectric layer and is consistent with a decrease in permittivity at low fields near E_c.[62] With further cycling domains may become pinned again due to an increasing number of immobilized charged defects. Domain de-pinning would increase the number of domains contributing to switching and subsequently increase the permittivity measured at saturating DC fields. However, the permittivity at saturating fields in both HZO-H_2O and HZO-O_2* did not change considerably after fatigue cycling. The behavior shown in Figure 6b is consistent with the seed inhibition mechanism which Colla et al. described as when small grains/regions of "ferroelectrically dead" material inhibit domain nucleation or lock domains in one polarization state.[63,68] The locking of domains in one polarization state near the electrode, or seeds, results in a decrease in polarization and permittivity without changes to the number of pinned domain walls. Though HZO-O_2* experienced a higher change in permittivity from its pristine to fatigued state, the capacitor experienced two decades more of field cycling. Thus, the effect of oxygen source was not found to alter the fatigue mechanism experienced by HZO but instead using O_2* instead of H_2O was found to increase the endurance limit and permittivity of HZO-O_2* capacitors.

■ CONCLUSIONS

We report the fabrication and characterization of TiN/HZO/TiN MFM capacitors grown using either O_2-plasma or H_2O during a fully *in situ* ALD procedure. Chemical analysis via ToF-SIMS shows the presence of a thicker interfacial oxide at the HZO/TiN interface for HZO-O_2* and is confirmed via TEM. GIXRD reveals that not only does the chemical interface change with ALD growth via different oxygen sources but the interfacial TiO_x layer, which is more heavily promoted by O_2*, may also promote the development of 111-fiber texture in HZO. Electrical investigation of both films reveals a slightly smaller P_r of 21 $\mu C/cm^2$ in HZO-O_2* compared to 25 $\mu C/cm^2$ in HZO-H_2O. Though switching kinetics measurements revealed a higher switching activation barrier in HZO-O_2* due to the more prominent interfacial oxide, HZO-O_2* demonstrated higher switching speeds and typical operating voltages, which may be more advantageous to next-generation ferroelectric memory applications.[60,69] In addition, HZO-O_2* demonstrates a higher endurance limit by up to 2 decades and lower leakage current density than HZO-H_2O. These results elucidate relevant processing−structure−property relationships in HZO films deposited via two different oxygen sources, H_2O and O_2-plasma, and demonstrate that selection of an oxygen source for ALD growth is an important consideration for the interface design of HZO thin films.

■ ASSOCIATED CONTENT

Supporting Information

The Supporting Information is available free of charge at https://pubs.acs.org/doi/10.1021/acsami.2c11073.

> Experimental details for GIXRD, XPS, ToF-SIMS, SEM, 2D-XRD, and switching kinetics measurements; high-resolution XPS data of C 1s, O 1s, Zr 3d, and Hf 4f spectra; and grain size estimation from SEM images (PDF)

■ AUTHOR INFORMATION

Corresponding Authors

Hanan Alexandra Hsain − *Materials Science and Engineering Department, North Carolina State University, Raleigh, North Carolina 27695, United States; NaMLab gGmbH, 01187 Dresden, Germany;* orcid.org/0000-0002-6745-829X; Email: hahsain@ncsu.edu

Jacob L. Jones − *Materials Science and Engineering Department, North Carolina State University, Raleigh, North Carolina 27695, United States;* orcid.org/0000-0002-9182-0957; Email: jacobjones@ncsu.edu

Authors

Younghwan Lee − *Materials Science and Engineering Department, North Carolina State University, Raleigh, North Carolina 27695, United States*

Suzanne Lancaster − *NaMLab gGmbH, 01187 Dresden, Germany;* orcid.org/0000-0002-5689-2795

Monica Materano − *NaMLab gGmbH, 01187 Dresden, Germany;* orcid.org/0000-0003-2039-2120

Ruben Alcala − *NaMLab gGmbH, 01187 Dresden, Germany*

Bohan Xu − *NaMLab gGmbH, 01187 Dresden, Germany;* orcid.org/0000-0001-7780-3424

Thomas Mikolajick − *NaMLab gGmbH, 01187 Dresden, Germany; TU Dresden, Chair of Nanoelectronics, 01187 Dresden, Germany;* orcid.org/0000-0003-3814-0378

Uwe Schroeder − *NaMLab gGmbH, 01187 Dresden, Germany;* orcid.org/0000-0002-6824-2386

Gregory N. Parsons − *Chemical and Biomolecular Engineering Department, North Carolina State University, Raleigh, North Carolina 27695, United States;* orcid.org/0000-0002-0048-5859

Complete contact information is available at: https://pubs.acs.org/10.1021/acsami.2c11073

Notes

The authors declare no competing financial interest.

■ ACKNOWLEDGMENTS

This work is based upon the work supported by the National Science Foundation (NSF), as part of the Center for Dielectrics and Piezoelectrics under grant nos. IIP-1841453 and IIP-1841466. H.A.H. was supported by the National Science Foundation Graduate Research Fellowship Program (no. DGE-1746939), an INTERN supplemental grant, and the IIE-GIRE Program funded by the National Science Foundation (no. 1829436). This work was performed at the Analytical Instrumentation Facility (AIF) at North Carolina State University and at the NC State Nanofabrication Facility (NNF), both of which are supported by the State of North Carolina and the National Science Foundation (Award No. ECCS-2025064). A.I.F. and N.N.F. are members of the North Carolina Research Triangle Nanotechnology Network (RTNN), a site in the National Nanotechnology Coordinated Infrastructure (NNCI). S.L. acknowledges funding from the FLAG-ERA JTC 2019 grant SOgraphMEM through the DFG (MI 1247/18-1). P.D.L., R.A., S.L., and B.X. acknowledge the support by the Deutsche Forschungs Gemeinschaft DFG within the following projects (Zeppelin (433647091) and HOMER (430054035)). U.S. and T.M. were financially supported out of the Saxonian State budget approved by the delegates of the Saxon State Parliament.

■ REFERENCES

(1) Valasek, J. Piezo-Electric and Allied Phenomena in Rochelle Salt. *Phys. Rev.* **1921**, *17*, 475−481.

(2) Hsain, H. A.; Lee, Y.; Materano, M.; Mittmann, T.; Payne, A.; Mikolajick, T.; Schroeder, U.; Parsons, G. N.; Jones, J. L. Many Routes to Ferroelectric HfO $_2$: A Review of Current Deposition Methods. *J. Vac. Sci. Technol., A* **2022**, *40*, No. 010803.

(3) Mueller, S.; Summerfelt, S. R.; Muller, J.; Schroeder, U.; Mikolajick, T. Ten-Nanometer Ferroelectric Si:HfO Films for Next-Generation FRAM Capacitors. *IEEE Electron Device Lett.* **2012**, *33*, 1300−1302.

(4) Muller, J.; Boscke, T. S.; Muller, S.; Yurchuk, E.; Polakowski, P.; Paul, J.; Martin, D.; Schenk, T.; Khullar, K.; Kersch, A.; Weinreich, W.; Riedel, S.; Seidel, K.; Kumar, A.; Arruda, T. M.; Kalinin, S. V.; Schlosser, T.; Boschke, R.; van Bentum, R.; Schroder, U.; Mikolajick, T. In *Ferroelectric Hafnium Oxide: A CMOS-Compatible and Highly Scalable Approach to Future Ferroelectric Memories*, 2013 IEEE International Electron Devices Meeting; IEEE: Washington, DC, USA, 2013; pp 10.8.1−10.8.4.

(5) Park, M. H.; Kim, H. J.; Kim, Y. J.; Moon, T.; Kim, K. D.; Hwang, C. S. Thin Hf_x Zr_{1-x} O_2 Films: A New Lead-Free System for Electrostatic Supercapacitors with Large Energy Storage Density and Robust Thermal Stability. *Adv. Energy Mater.* **2014**, *4*, No. 1400610.

(6) Park, M. H.; Kim, H. J.; Kim, Y. J.; Moon, T.; Kim, K. D.; Lee, Y. H.; Hyun, S. D.; Hwang, C. S. Giant Negative Electrocaloric Effects of $Hf_{0.5}Zr_{0.5}O_2$ Thin Films. *Adv. Mater.* **2016**, *28*, 7956−7961.

(7) Ryu, H.; Wu, H.; Rao, F.; Zhu, W. Ferroelectric Tunneling Junctions Based on Aluminum Oxide/ Zirconium-Doped Hafnium Oxide for Neuromorphic Computing. *Sci. Rep.* **2019**, *9*, No. 20383.

(8) Gao, Z.; Luo, Y.; Lyu, S.; Cheng, Y.; Zheng, Y.; Zhong, Q.; Zhang, W.; Lyu, H. Identification of Ferroelectricity in a Capacitor With Ultra-Thin (1.5-Nm) $Hf_{0.5}Zr_{0.5}O_2$ Film. *IEEE Electron Device Lett.* **2021**, *42*, 1303−1306.

(9) Böscke, T. S.; Müller, J.; Bräuhaus, D.; Schröder, U.; Böttger, U. Ferroelectricity in Hafnium Oxide Thin Films. *Appl. Phys. Lett.* **2011**, *99*, No. 102903.

(10) Lee, D. H.; Lee, Y.; Yang, K.; Park, J. Y.; Kim, S. H.; Reddy, P. R. S.; Materano, M.; Mulaosmanovic, H.; Mikolajick, T.; Jones, J. L.; Schroeder, U.; Park, M. H. Domains and Domain Dynamics in Fluorite-Structured Ferroelectrics. *Appl. Phys. Rev.* **2021**, *8*, No. 021312.

(11) Batra, R.; Tran, H. D.; Ramprasad, R. Stabilization of Metastable Phases in Hafnia Owing to Surface Energy Effects. *Appl. Phys. Lett.* **2016**, *108*, No. 172902.

(12) Xu, X.; Huang, F.-T.; Qi, Y.; Singh, S.; Rabe, K. M.; Obeysekera, D.; Yang, J.; Chu, M.-W.; Cheong, S.-W. Kinetically Stabilized Ferroelectricity in Bulk Single-Crystalline HfO2:Y. *Nat. Mater.* **2021**, *20*, 826−832.

(13) Müller, J.; Böscke, T. S.; Schröder, U.; Mueller, S.; Bräuhaus, D.; Böttger, U.; Frey, L.; Mikolajick, T. Ferroelectricity in Simple Binary ZrO_2 and HfO_2. *Nano Lett.* **2012**, *12*, 4318−4323.

(14) Hsain, H. A.; Lee, Y.; Parsons, G.; Jones, J. L. Compositional Dependence of Crystallization Temperatures and Phase Evolution in Hafnia-Zirconia $(Hf_xZr_{1-x})O_2$ Thin Films. *Appl. Phys. Lett.* **2020**, *116*, No. 192901.

(15) Park, M. H.; Schenk, T.; Fancher, C. M.; Grimley, E. D.; Zhou, C.; Richter, C.; LeBeau, J. M.; Jones, J. L.; Mikolajick, T.; Schroeder, U. A Comprehensive Study on the Structural Evolution of HfO_2 Thin Films Doped with Various Dopants. *J. Mater. Chem. C* **2017**, *5*, 4677−4690.

(16) Lee, Y.; Alex Hsain, H.; Fields, S. S.; Jaszewski, S. T.; Horgan, M. D.; Edgington, P. G.; Ihlefeld, J. F.; Parsons, G. N.; Jones, J. L. Unexpectedly Large Remanent Polarization of $Hf_{0.5}Zr_{0.5}O_2$ Metal−Ferroelectric−Metal Capacitor Fabricated without Breaking Vacuum. *Appl. Phys. Lett.* **2021**, *118*, No. 012903.

(17) Richter, C.; Schenk, T.; Schroeder, U.; Mikolajick, T. Film Properties of Low Temperature HfO_2 Grown with H2O, O3, or Remote O_2 -Plasma. *J. Vac. Sci. Technol., A* **2014**, *32*, No. 01A117.

(18) Aarik, J.; Aidla, A.; Kikas, A.; Käämbre, T.; Rammula, R.; Ritslaid, P.; Uustare, T.; Sammelselg, V. Effects of Precursors on Nucleation in Atomic Layer Deposition of HfO2. *Appl. Surf. Sci.* **2004**, *230*, 292−300.

(19) Lo Nigro, R.; Schilirò, E.; Mannino, G.; Di Franco, S.; Roccaforte, F. Comparison between Thermal and Plasma Enhanced Atomic Layer Deposition Processes for the Growth of HfO2 Dielectric Layers. *J. Crystal Growth* **2020**, *539*, No. 125624.

(20) Alcala, R.; Richter, C.; Materano, M.; Lomenzo, P. D.; Zhou, C.; Jones, J. L.; Mikolajick, T.; Schroeder, U. Influence of Oxygen Source on the Ferroelectric Properties of ALD Grown $Hf_{1-x}Zr_xO_2$ Films. *J. Phys. D: Appl. Phys.* **2021**, *54*, No. 035102.

(21) Kim, S. J.; Mohan, J.; Kim, H. S.; Lee, J.; Hwang, S. M.; Narayan, D.; Lee, J.-G.; Young, C. D.; Colombo, L.; Goodman, G.; Wan, A. S.; Cha, P.-R.; Summerfelt, S. R.; San, T.; Kim, J. Effect of Hydrogen Derived from Oxygen Source on Low-Temperature Ferroelectric TiN/$Hf_{0.5}Zr_{0.5}O_2$/TiN Capacitors. *Appl. Phys. Lett.* **2019**, *115*, No. 182901.

(22) Grimley, E. D.; Schenk, T.; Mikolajick, T.; Schroeder, U.; LeBeau, J. M. Atomic Structure of Domain and Interphase Boundaries in Ferroelectric HfO_2. *Adv. Mater. Interfaces* **2018**, *5*, No. 1701258.

(23) Das, K. C.; Tripathy, N.; Ghosh, S. P.; Sharma, P.; Singhal, R.; Kar, J. P. Microstructural, Surface and Interface Properties of Zirconium Doped HfO_2 Thin Films Grown by RF Co-Sputtering Technique. *Vacuum* **2017**, *143*, 288−293.

(24) Lin, Y.; Chen, C. L. Interface Effects on Highly Epitaxial Ferroelectric Thin Films. *J. Mater. Sci.* **2009**, *44*, 5274−5287.

(25) Hamouda, W.; Pancotti, A.; Lubin, C.; Tortech, L.; Richter, C.; Mikolajick, T.; Schroeder, U.; Barrett, N. Physical Chemistry of the TiN/$Hf_{0.5}Zr_{0.5}O_2$ Interface. *J. Appl. Phys.* **2020**, *127*, No. 064105.

(26) Baumgarten, L.; Szyjka, T.; Mittmann, T.; Materano, M.; Matveyev, Y.; Schlueter, C.; Mikolajick, T.; Schroeder, U.; Müller, M. Impact of Vacancies and Impurities on Ferroelectricity in PVD- and ALD-Grown HfO_2 Films. *Appl. Phys. Lett.* **2021**, *118*, No. 032903.

(27) Kim, K. D.; Park, M. H.; Kim, H. J.; Kim, Y. J.; Moon, T.; Lee, Y. H.; Hyun, S. D.; Gwon, T.; Hwang, C. S. Ferroelectricity in Undoped-HfO_2 Thin Films Induced by Deposition Temperature Control during Atomic Layer Deposition. *J. Mater. Chem. C* **2016**, *4*, 6864−6872.

(28) Esteves, G.; Ramos, K.; Fancher, C.; Jones, J. *LIPRAS (Line-Profile Analysis Software)*; LIPRAS, 2017.

(29) Grimley, E. D.; Schenk, T.; Sang, X.; Pešić, M.; Schroeder, U.; Mikolajick, T.; LeBeau, J. M. Structural Changes Underlying Field-Cycling Phenomena in Ferroelectric HfO_2 Thin Films. *Adv. Electron. Mater.* **2016**, *2*, No. 1600173.

(30) Christensen, A.; Carter, E. A. First-Principles Study of the Surfaces of Zirconia. *Phys. Rev. B* **1998**, *58*, 8050−8064.

(31) Schenk, T.; Fancher, C. M.; Park, M. H.; Richter, C.; Künneth, C.; Kersch, A.; Jones, J. L.; Mikolajick, T.; Schroeder, U. On the Origin of the Large Remanent Polarization in La:HfO_2. *Adv. Electron. Mater.* **2019**, *5*, No. 1900303.

(32) Fields, S. S.; Olson, D. H.; Jaszewski, S. T.; Fancher, C. M.; Smith, S. W.; Dickie, D. A.; Esteves, G.; Henry, M. D.; Davids, P. S.; Hopkins, P. E.; Ihlefeld, J. F. Compositional and Phase Dependence of Elastic Modulus of Crystalline and Amorphous $Hf_{1-x}Zr_xO_2$ Thin Films. *Appl. Phys. Lett.* **2021**, *118*, No. 102901.

(33) Shiraishi, T.; Choi, S.; Kiguchi, T.; Shimizu, T.; Funakubo, H.; Konno, T. J. Formation of the Orthorhombic Phase in CeO_2-HfO_2 Solid Solution Epitaxial Thin Films and Their Ferroelectric Properties. *Appl. Phys. Lett.* **2019**, *114*, No. 232902.

(34) Cao, R.; Wang, Y.; Zhao, S.; Yang, Y.; Zhao, X.; Wang, W.; Zhang, X.; Lv, H.; Liu, Q.; Liu, M. Effects of Capping Electrode on Ferroelectric Properties of $Hf_{0.5}Zr_{0.5}O_2$ Thin Films. *IEEE Electron Device Lett.* **2018**, *39*, 1207−1210.

(35) Cen, Z. H.; Xu, B. X.; Hu, J. F.; Ji, R.; Toh, Y. T.; Ye, K. D.; Hu, Y. F. Temperature Effect on Titanium Nitride Nanometer Thin Film in Air. *J. Phys. D: Appl. Phys.* **2017**, *50*, No. 075105.

(36) Hummer, D. R.; Heaney, P. J.; Post, J. E. Thermal Expansion of Anatase and Rutile between 300 and 575 K Using Synchrotron Powder X-Ray Diffraction. *Powder Diffr.* **2007**, *22*, 352−357.

(37) Estandía, S.; Dix, N.; Gazquez, J.; Fina, I.; Lyu, J.; Chisholm, M. F.; Fontcuberta, J.; Sánchez, F. Engineering Ferroelectric $Hf_{0.5}Zr_{0.5}O_2$ Thin Films by Epitaxial Stress. *ACS Appl. Electron. Mater.* **2019**, *1*, 1449−1457.

(38) Tagantsev, A. K.; Landivar, M.; Colla, E.; Setter, N. Identification of Passive Layer in Ferroelectric Thin Films from Their Switching Parameters. *J. Appl. Phys.* **1995**, *78*, 2623−2630.

(39) Materano, M.; Lomenzo, P. D.; Kersch, A.; Park, M. H.; Mikolajick, T.; Schroeder, U. Interplay between Oxygen Defects and Dopants: Effect on Structure and Performance of HfO_2-Based Ferroelectrics. *Inorg. Chem. Front.* **2021**, *8*, 2650−2672.

(40) Park, M. H.; Lee, D. H.; Yang, K.; Park, J.-Y.; Yu, G. T.; Park, H. W.; Materano, M.; Mittmann, T.; Lomenzo, P. D.; Mikolajick, T.; Schroeder, U.; Hwang, C. S. Review of Defect Chemistry in Fluorite-Structure Ferroelectrics for Future Electronic Devices. *J. Mater. Chem. C* **2020**, *8*, 10526−10550.

(41) Weinreich, W.; Shariq, A.; Seidel, K.; Sundqvist, J.; Paskaleva, A.; Lemberger, M.; Bauer, A. J. Detailed Leakage Current Analysis of Metal−Insulator−Metal Capacitors with ZrO2, ZrO2/SiO2/ZrO2, and ZrO2/Al2O3/ZrO2 as Dielectric and TiN Electrodes. *J. Vac. Sci. Technol., B: Nanotechnol. Microelectron.: Mater., Process., Meas., Phenom.* **2013**, *31*, No. 01A109.

(42) Szyjka, T.; Baumgarten, L.; Mittmann, T.; Matveyev, Y.; Schlueter, C.; Mikolajick, T.; Schroeder, U.; Müller, M. Enhanced Ferroelectric Polarization in TiN/HfO_2/TiN Capacitors by Interface Design. *ACS Appl. Electron. Mater.* **2020**, *2*, 3152−3159.

(43) Chen, B.; Yang, H.; Zhao, L.; Miao, J.; Xu, B.; Qiu, X. G.; Zhao, B. R.; Qi, X. Y.; Duan, X. F. Thickness and Dielectric Constant of Dead Layer in Pt/(Ba0.7Sr0.3)TiO3/YBa2Cu3O7−x Capacitor. *Appl. Phys. Lett.* **2004**, *84*, 583−585.

(44) Podgorny, Yu. V.; Vorotilov, K. A.; Sigov, A. S.; Scott, J. F. Dead Layer Thickness Estimation at the Ferroelectric Film-Metal Interface in PZT. *Appl. Phys. Lett.* **2019**, *114*, No. 132902.

(45) Tomczyk, M.; Mahajan, A.; Tkach, A.; Vilarinho, P. M. Interface-Based Reduced Coercivity and Leakage Currents of BiFeO3 Thin Films: A Comparative Study. *Mater. Des.* **2018**, *160*, 1322−1334.

(46) Materano, M.; Lomenzo, P. D.; Mulaosmanovic, H.; Hoffmann, M.; Toriumi, A.; Mikolajick, T.; Schroeder, U. Polarization Switching in Thin Doped HfO_2 Ferroelectric Layers. *Appl. Phys. Lett.* **2020**, *117*, No. 262904.

(47) Setter, N.; Damjanovic, D.; Eng, L.; Fox, G.; Gevorgian, S.; Hong, S.; Kingon, A.; Kohlstedt, H.; Park, N. Y.; Stephenson, G. B.; Stolitchnov, I.; Taganstev, A. K.; Taylor, D. V.; Yamada, T.; Streiffer, S. Ferroelectric Thin Films: Review of Materials, Properties, and Applications. *J. Appl. Phys.* **2006**, *100*, No. 051606.

(48) Tagantsev, A. K.; Stolichnov, I.; Setter, N.; Cross, J. S.; Tsukada, M. Non-Kolmogorov-Avrami Switching Kinetics in Ferroelectric Thin Films. *Phys. Rev. B* **2002**, *66*, No. 214109.

(49) Du, X.; Chen, I.-W. Frequency Spectra of Fatigue of PZT and Other Ferroelectric Thin Films. *MRS Proc.* **1997**, *493*, No. 311.

(50) Mulaosmanovic, H.; Ocker, J.; Müller, S.; Schroeder, U.; Müller, J.; Polakowski, P.; Flachowsky, S.; van Bentum, R.; Mikolajick, T.; Slesazeck, S. Switching Kinetics in Nanoscale Hafnium Oxide Based Ferroelectric Field-Effect Transistors. *ACS Appl. Mater. Interfaces* **2017**, *9*, 3792−3798.

(51) Mulaosmanovic, H.; Muller, F.; Lederer, M.; Ali, T.; Hoffmann, R.; Seidel, K.; Zhou, H.; Ocker, J.; Mueller, S.; Dunkel, S.; Kleimaier, D.; Muller, J.; Trentzsch, M.; Beyer, S.; Breyer, E. T.; Mikolajick, T.; Slesazeck, S. Interplay Between Switching and Retention in HfO$_2$-Based Ferroelectric FETs. *IEEE Trans. Electron Devices* **2020**, *67*, 3466−3471.

(52) Wieder, H. H. Activation Field and Coercivity of Ferroelectric Barium Titanate. *J. Appl. Phys.* **1957**, *28*, 367−369.

(53) Lee, H.-J.; Lee, M.; Lee, K.; Jo, J.; Yang, H.; Kim, Y.; Chae, S. C.; Waghmare, U.; Lee, J. H. Scale-Free Ferroelectricity Induced by Flat Phonon Bands in HfO$_2$. *Science* **2020**, *369*, 1343−1347.

(54) Choudhury, S.; Li, Y.; Odagawa, N.; Vasudevarao, A.; Tian, L.; Capek, P.; Dierolf, V.; Morozovska, A. N.; Eliseev, E. A.; Kalinin, S.; Cho, Y.; Chen, L.; Gopalan, V. The Influence of 180° Ferroelectric Domain Wall Width on the Threshold Field for Wall Motion. *J. Appl. Phys.* **2008**, *104*, No. 084107.

(55) Park, H. W.; Hyun, S. D.; Lee, I. S.; Lee, S. H.; Lee, Y. B.; Oh, M.; Kim, B. Y.; Ryoo, S. G.; Hwang, C. S. Polarizing and Depolarizing Charge Injection through a Thin Dielectric Layer in a Ferroelectric−Dielectric Bilayer. *Nanoscale* **2021**, *13*, 2556−2572.

(56) Jiang, A. Q.; Lee, H. J.; Kim, G. H.; Hwang, C. S. The Inlaid Al$_2$O$_3$ Tunnel Switch for Ultrathin Ferroelectric Films. *Adv. Mater.* **2009**, *21*, 2870−2875.

(57) Lee, Y. *Interface Engineering of Ferroelectric Hf0.5Zr0.5O2 Metal-Ferroelectric-Metal Capacitors*; NC State University: Raleigh, North Carolina, 2022.

(58) Wallace, M.; Johnson-Wilke, R. L.; Esteves, G.; Fancher, C. M.; Wilke, R. H. T.; Jones, J. L.; Trolier-McKinstry, S. In Situ Measurement of Increased Ferroelectric/Ferroelastic Domain Wall Motion in Declamped Tetragonal Lead Zirconate Titanate Thin Films. *J. Appl. Phys.* **2015**, *117*, No. 054103.

(59) Esteves, G.; Wallace, M.; Johnson-Wilke, R.; Fancher, C. M.; Wilke, R. H. T.; Trolier-McKinstry, S.; Jones, J. L. Effect of Mechanical Constraint on Domain Reorientation in Predominantly {111}-Textured Lead Zirconate Titanate Films. *J. Am. Ceram. Soc.* **2016**, *99*, 1802−1807.

(60) Kim, S. J.; Mohan, J.; Young, C. D.; Colombo, L.; Kim, J.; Summerfelt, S. R.; San, T. In *Ferroelectric TiN/Hf0.5Zr0.5O2/TiN Capacitors with Low-Voltage Operation and High Reliability for Next-Generation FRAM Applications*, 2018 IEEE International Memory Workshop (IMW); IEEE: Kyoto, 2018; pp 1−4.

(61) Okuno, J.; Kunihiro, T.; Konishi, K.; Maemura, H.; Shuto, Y.; Sugaya, F.; Materano, M.; Ali, T.; Kuehnel, K.; Seidel, K.; Schroeder, U.; Mikolajick, T.; Tsukamoto, M.; Umebayashi, T. In *SoC Compatible 1T1C FeRAM Memory Array Based on Ferroelectric Hf0.5Zr0.5O2*, 2020 IEEE Symposium on VLSI Technology; IEEE: Honolulu, HI, USA, 2020; pp 1−2.

(62) Warren, W. L.; Dimos, D.; Tuttle, B. A.; Nasby, R. D.; Pike, G. E. Electronic Domain Pinning in Pb(Zr,Ti)O$_3$ Thin Films and Its Role in Fatigue. *Appl. Phys. Lett.* **1994**, *65*, 1018−1020.

(63) Colla, E. L.; Taylor, D. V.; Tagantsev, A. K.; Setter, N. Discrimination between Bulk and Interface Scenarios for the Suppression of the Switchable Polarization (Fatigue) in Pb(Zr,Ti)O3 Thin Films Capacitors with Pt Electrodes. *Appl. Phys. Lett.* **1998**, *72*, 2478−2480.

(64) Pešić, M.; Fengler, F. P. G.; Larcher, L.; Padovani, A.; Schenk, T.; Grimley, E. D.; Sang, X.; LeBeau, J. M.; Slesazeck, S.; Schroeder, U.; Mikolajick, T. Physical Mechanisms behind the Field-Cycling Behavior of HfO$_2$-Based Ferroelectric Capacitors. *Adv. Funct. Mater.* **2016**, *26*, 4601−4612.

(65) Laha, A.; Ai, B.; Babu, P. R. P.; Fissel, A.; Osten, H. J. Impact of Carbon Incorporation into Epitaxial Gd$_2$O$_3$ Thin Films on Silicon: An Experimental Study on Electrical Properties. *Appl. Phys. Lett.* **2011**, *99*, No. 152902.

(66) Kim, K.-M.; Jang, J. S.; Yoon, S.-G.; Yun, J.-Y.; Chung, N.-K. Structural, Optical and Electrical Properties of HfO2 Thin Films Deposited at Low-Temperature Using Plasma-Enhanced Atomic Layer Deposition. *Materials* **2020**, *13*, No. 2008.

(67) Materlik, R.; Künneth, C.; Kersch, A. The Origin of Ferroelectricity in Hf$_{1-x}$Zr$_x$O$_2$: A Computational Investigation and a Surface Energy Model. *J. Appl. Phys.* **2015**, *117*, No. 134109.

(68) Bolten, D.; Böttger, U.; Waser, R. Reversible and Irreversible Polarization Processes in Ferroelectric Ceramics and Thin Films. *J. Appl. Phys.* **2003**, *93*, 1735−1742.

(69) Kim, S. J.; Mohan, J.; Kim, H. S.; Lee, J.; Young, C. D.; Colombo, L.; Summerfelt, S. R.; San, T.; Kim, J. Low-Voltage Operation and High Endurance of 5-Nm Ferroelectric Hf$_{0.5}$Zr$_{0.5}$O$_2$ Capacitors. *Appl. Phys. Lett.* **2018**, *113*, No. 182903.